

# Axiverse Machine

Masha Baryakhtar, David Cyncynates, Ella Henry

August 18, 2025

## 1 Anthropics

The bounds for the possible ratio of the dark matter abundance to baryon abundance,  $\zeta$ , are given in [1] to be  $2.5 < \zeta < 100$ . The lower bound is related to the value for which perturbations near the size of our galaxy’s stop growing, and the upper bound is related to the value that ultimately prevents star formation. All values within this range are allowed in the sense that they would lead to our existence today, but their likelihoods depend on the theory for dark matter, as we will see below. In section 5 of [2], the authors consider the case of  $n$  axions and the fraction of the dark matter that they constitute. If the axions make up all of the dark matter, then we can write  $\zeta$  as:

$$\zeta = \sum_{a=1}^n c(m_a) F(\theta_a) \tag{1}$$

Here,  $c(m_a)F(\theta_a)$  is the fractional abundance in the  $a$ -th axion, where  $F(\theta_a)$  encodes the dependence of the fractional abundance on the axion’s initial misalignment angle. For small enough angles,  $F(\theta_a) \sim \theta_a^2$ . The  $c(m_a)$  factor takes into account the fractional abundance’s dependence on the mass and on the scale of symmetry breaking, e.g. for axions that start to oscillate during radiation domination,  $c(m_a) \sim \left(\frac{m_a}{H_{eq}}\right)^{1/2} \left(\frac{f_a}{M_{pl}}\right)^2$ .

### 1.1 The anthropic measure

The authors of [2] then calculate the probability  $P$  of finding ourselves in a causal patch where the dark matter abundance is no larger than the observed value of  $\zeta \sim 5$ , without being so small that we could not exist, in other words, the probability that  $2.5 < \zeta < 5$ . The calculation uses the causal diamond measure (details in [1]) to circumvent the problem of computing probabilities in an infinite-dimensional space, which leads to difficulties in normalizing these probabilities. The measure allows us to restrict ourselves to one causal patch and consider the number of observations made in that patch. To determine this number, the author of [1] counts the number of baryons in a causal patch and then the number of observations per baryon. The quantitative expression

the author finds for the number of baryons in a causal patch is  $(1 + \zeta)^{-1}$  with the assumption of fixed baryon-to-photon ratio. The number of observers per baryon is approximated to be constant within the range of allowed  $\zeta$  values. The overall contribution to the probability density from the causal diamond measure is therefore  $C(1 + \zeta)^{-1}$ , for some constant  $C$ .

We must also assume some distribution for the initial conditions  $\theta_a$ , which will depend on the scale of inflation relative to the axion's potential: for high scale inflation, the distribution is flat between  $[-\pi, \pi]$ , while for low scale inflation,  $p(\theta_a) \propto \exp\left(-\frac{8\pi^2 V(\theta_a)}{3H^4}\right)$ , where  $V(\theta_a) = \Lambda^4(1 - \cos\theta_a)$ . We can approximate this distribution from low scale inflation as flat between  $[-\sigma, \sigma]$ , where  $\sigma^2 = 3H^4/(8\pi^2 m^2 f^2)$  is the spread in this distribution. So in general, we can consider  $p(\theta_a)$  to be flat between two values, which we'll call  $\pm f(H)$ , where:

$$f(H) = \begin{cases} \pi & \text{for } H > \Lambda \\ \sigma & \text{for } H < \Lambda \end{cases} \quad (2)$$

Now, using the causal diamond measure described above and the flat distribution between  $\pm f(H)$  for the initial conditions, we can write down an expression for the probability  $P$ :

$$P = N^{-1} \frac{C}{(2f(H))^n} \int_{2.5 < \zeta(\theta_a) < 5} \frac{\prod_{a=1}^n d\theta_a}{1 + \zeta(\theta_a)} \quad (3)$$

where again  $n$  is the number of axions and  $C$  is the constant factor from the number of observations per baryon. The normalization  $N$  is such that the probability is normalized to 1 and is given by:

$$N = \frac{C}{(2f(H))^n} \int_{2.5 < \zeta(\theta_a) < 100} \frac{\prod_{a=1}^n d\theta_a}{1 + \zeta(\theta_a)} \quad (4)$$

We can compute this probability for any value of  $f(H)$  by rescaling the integration variables as  $\theta'_a = \theta_a/f(H)$  and writing  $\zeta(\theta_a) = c_a \theta_a^2$  (summing over the  $a$  index):

$$P = \mathcal{N}^{-1} \int_{-1}^1 \frac{\prod_{a=1}^n d\theta'_a}{1 + c'_a \theta'^2_a} \Theta(c'_a \theta'^2_a - 2.5) \Theta(5 - c'_a \theta'^2_a) \quad (5)$$

where the  $\theta_a$ -independent factors out front in Eq. (3) have canceled out with those in the normalization  $N$ , and so  $\mathcal{N}$  is the same as  $N$ , without those factors.  $\Theta$  here is the Heaviside function and  $c'_a \equiv c_a f(H)^2$ .

## 1.2 1 axion

The probability for one axion is given by Eq. (5) for  $n = 1$  and can be computed numerically as a function of  $c'_1$ . It is plotted below:

Fig. 1 shows that once  $c'_1 > \zeta_{\text{upper}} = 100$ , the probability becomes independent of the axion parameters (recall that  $c' \propto m^{1/2} f^2$ ), and acquires the

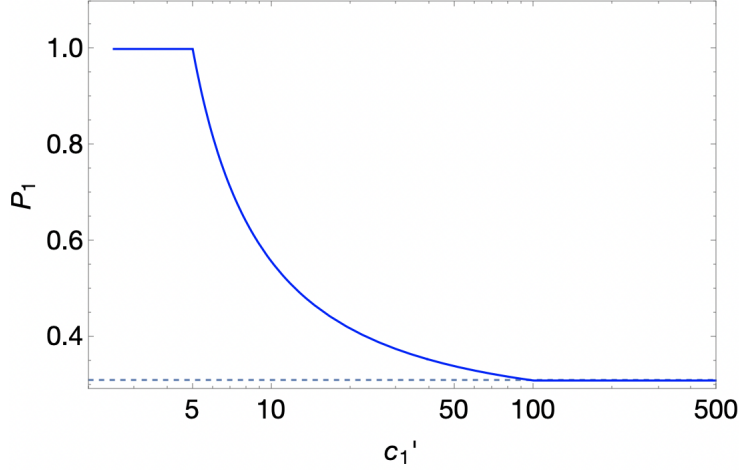


Figure 1: Probability of measuring  $2.5 < \zeta < 5$  in the case of one axion, as a function of  $c_1'$ . The dashed horizontal line corresponds to  $P = 0.3$ , the probability found for 1 axion in [2]

constant value of  $P = 0.3$ . This corresponds to the  $n = 1$  case of the result presented in Eq. 79 of [2], reproduced below:

$$P_n = \frac{\int_{2.5}^5 \frac{d\zeta \zeta^{(n-2)/2}}{1+\zeta}}{\int_{2.5}^{100} \frac{d\zeta \zeta^{(n-2)/2}}{1+\zeta}} = 0.3, 0.16, 0.06, 0.02, 0.006, \dots \quad (6)$$

In this result, the authors focus on  $n$  axions at the GUT scale ( $f \sim 10^{16}$  GeV), with masses heavy enough ( $m_a \geq 10^{-19}$  eV) so that the axions would find themselves in this constant  $P$  regime. Indeed, one can check that for  $f \sim 10^{16}$  GeV and  $m_a \geq 10^{-19}$  eV, the criterion  $c_a > 100$  is satisfied.

### 1.2.1 Exact anthropic probability with low scale inflation

In Section 1.2, we used an approximate form for the distribution of initial conditions from low scale inflation. We can compute the anthropic probability *for one axion* more precisely in the case of low scale inflation by numerically calculating the following:

$$P = N^{-1} \int_{2.5 < \zeta < 5} \frac{d\theta}{1+\zeta} \exp\left(-\frac{8\pi^2 V(\theta)}{3H^4}\right) \quad (7)$$

where the normalization is the same integral but with integration bound  $2.5 < \zeta < 100$ . This probability is plotted against  $\sqrt{mf}$  for certain values of  $H$  in Fig. 2 (and  $f$  is set to 1).

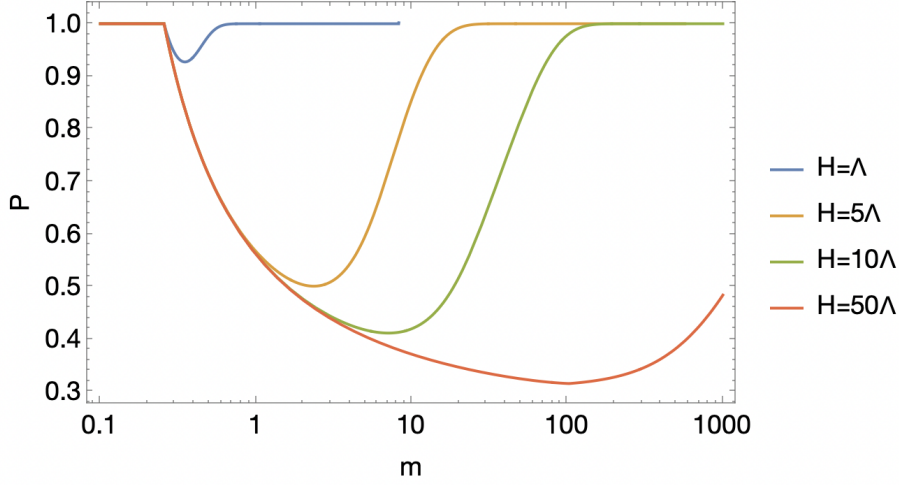


Figure 2: Probability of  $2.5 < \zeta < 5$  for a stochastic axion scenario (low scale, long-lasting inflation), with different values of  $H$  relative to  $\Lambda = (mf)^{1/2}$ . In this plot,  $f = 1$ .

As expected, for each curve, we see that when the scale of inflation is low relative to the size of the potential (i.e.  $H < \Lambda$ ), the probability that  $2.5 < \zeta < 5$  grows, since you are sampling  $\theta$  from a distribution peaked closer and closer to zero (effectively acts like a small  $c$ ). When  $H > \Lambda$ , you recover the expected behavior from flat initial conditions: the probability drops as  $\Lambda$  increases (until  $\Lambda \sim H$ , and then you enter the first regime).

### 1.3 2 axions

We can numerically compute the probability in Eq. (5) now for  $n = 2$ , and plot the results as a function of  $c'_2$ , for a few chosen values of  $c'_1$ . This is shown below in Fig. 3

The behavior of  $P_2$  shows that there is a little more nuance, but the result that an axion contributes to the anthropic measure once  $c' > \zeta_{\text{upper}}$  holds true. We see that if  $c'_1 \ll \zeta_{\text{upper}}$  and  $c'_2 > \zeta_{\text{upper}}$  (see red line for larger  $c'_2$  in Fig. 3), then the first axion does not contribute while the second one does, and thus we recover the  $P = 0.3$  probability from the 1-axion scenario. The same is true if  $c'_1 > \zeta_{\text{upper}}$  and  $c'_2 \ll \zeta_{\text{upper}}$  (Fig. 3, blue line for small  $c'_2$ ). If both  $c'_1, c'_2 > \zeta_{\text{upper}}$  (Fig. 3, blue line for large  $c'_2$ ), then the two axions contribute to the measure and so the probability is  $P = 0.16$ , in agreement with Eq. (6). There is a weird middle regime (purple line in Fig. 3, as well as region in all three lines where there is a bump), where I am not really sure what's going on yet.

We have thus seen, in the case of 1 and 2 axions, that the condition that an axion must satisfy to contribute to the anthropic measure is  $c' > \zeta_{\text{upper}}$ .

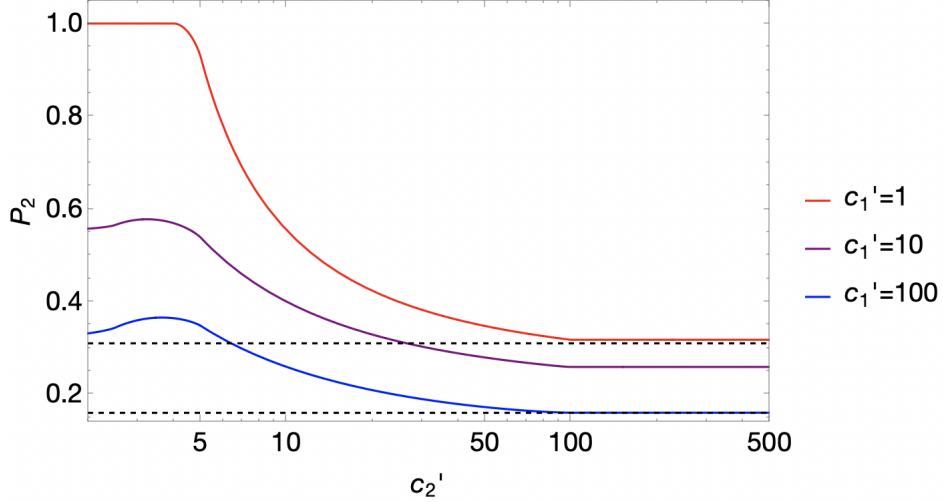


Figure 3: Probability of measuring  $2.5 < \zeta < 5$  in the case of two axion as a function of  $c_2'$ , for different values of  $c_1'$ . The dashed horizontal lines correspond to the probabilities for 1 and 2 axions as given by Eq. (6): 0.3 and 0.16 respectively.

Recalling that  $c' = c f(H)^2$  (with  $f(H)$  given in Eq. (2)), and that  $c = (m/H_{eq})^{1/2}(f/M_{pl})^2$  we can write this condition in terms of the physical parameters as:

$$\left(\frac{m}{H_{eq}}\right)^{1/2} \left(\frac{f}{M_{pl}}\right)^2 \min\left\{\pi^2, \frac{3H^4}{8\pi^2 m^2 f^2}\right\} > \zeta_{\text{upper}} \quad (8)$$

The takeaway is that if the scale of inflation is low, heavier axions will evade this criterion and therefore will not contribute to the anthropic measure: including them in the theory does not require more fine-tuning. On the other hand, if the scale of inflation is high, these axions will quickly satisfy this condition and require fine-tuning, while lighter axions won't (the words “lighter” and “heavier” depend on the values of  $H$  and  $f$  in each case respectively; this will need to be further investigated).

Note that Eq. (8) is approximate in that: (1) it assumes that  $F(\theta_a) \sim \theta^2$ , which is not true if  $\theta_a \sim O(1)$ , in which case there is a small correction; (2) it approximates the distribution of  $\theta_a$  in a low scale inflation scenario to be flat between  $\pm\sigma$ , instead of treating it fully as  $\propto \exp(-V(\theta_a)/H^4)$ ; and (3) it only accounts for regimes where  $H < \Lambda$  or  $H > \Lambda$ , and glosses over the  $H \sim \Lambda$  regime.

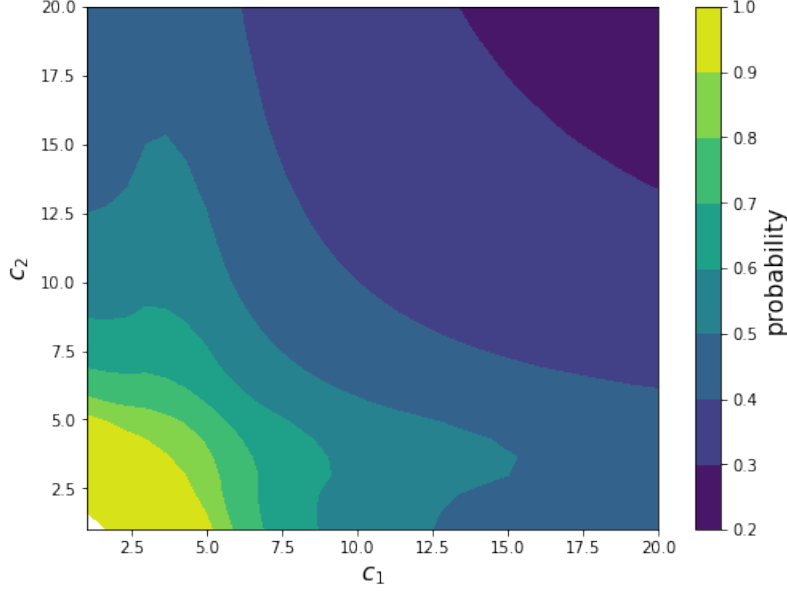


Figure 4: Contour plot for the probability shown in Fig. 3 as a function of  $c_1$  and  $c_2$  (numerically plotted, not amazing resolution and only up to  $c = 20$ )

### 1.3.1 Geometric interpretation

The challenge of computing the integrals in Eq. (5) comes from the bounds of integration: the integrand is integrated over each angle  $\theta_a$  from  $-1$  to  $1$ , but the integrand is only nonzero for  $2.5 < \sum_a c_a \theta_a^2 < b$ , where  $b = 5$  for the numerator in Eq. (5) and  $b = 100$  in the normalization.

To understand what this region of integration looks like, let's go back to the case of 2 axions. In the 2-dimensional space defined by the variables  $\theta_1$  and  $\theta_2$ , the area over which the two dimensional integral in Eq. (5) is to be computed corresponds to that of an elliptical ring (the  $2.5 < c_1 \theta_1^2 + c_2 \theta_2^2 < b$  constraint), cut off by a square of side length 2 (the bounds of integration for each angle). If  $c_1 > c_2$ , the semi-major axis of the inner (outer) ellipse is determined by  $2.5/c_1$  ( $b/c_1$ ), while the semi-minor axis of the inner (outer) ellipse is given by  $2.5/c_2$  ( $b/c_2$ ). The values of  $c_1$  and  $c_2$  therefore determine the size of the elliptical ring. This area is illustrated in Fig. 5 for a few choices of  $c_1$  and  $c_2$ .

While ultimately each point on the integration region will be weighted by the integrand (points away from the origin will carry less weight), having a sense of how this region is altered as  $c_1$  and  $c_2$  vary is important in understanding the resulting integral. There are a few regimes of interest that we will see can be mapped onto the behavior that appears in Fig. 3. These depend on regions of integration of both the numerator and normalization integrals. These are:

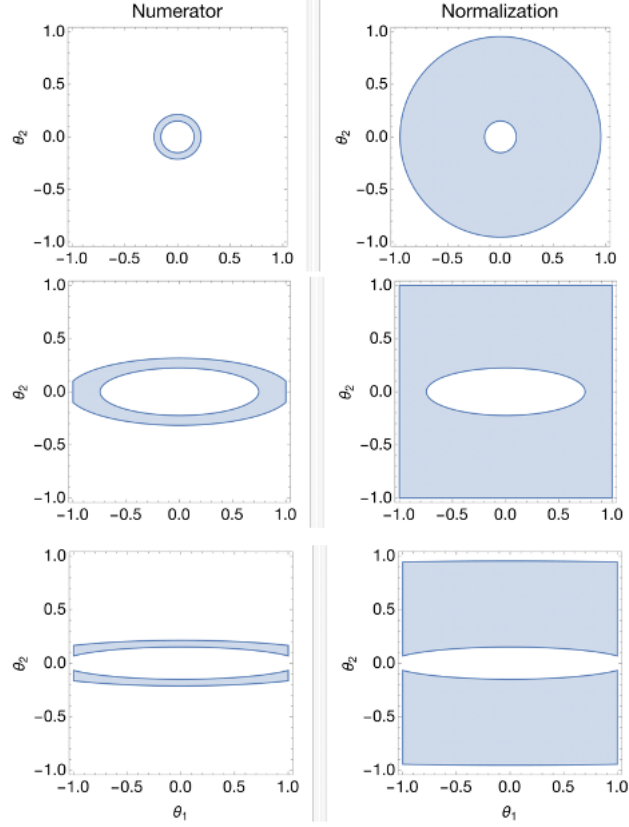


Figure 5: (this is a bad figure but just for illustrative purposes for now) First row corresponds to  $c_1 = 100, c_2 = 110$ ; middle row is  $c_1 = 4.5, c_2 = 50$ ; bottom row is  $c_1 = 2, c_2 = 110$ .

1. **when the elliptical ring is fully inside the square in both integrals:** This happens when either  $c_1$  or  $c_2 > 100$ . This is set by the value of semi-major(minor) axes needed for the ellipses to fit inside the square in both integrals. This case corresponds to the case where the axions are heavy enough that they contribute to the anthropic measure, i.e. the result from [2] given in Eq. (6). The result of the integrations is independent of the  $c$ 's, since the dependence cancels out in numerator and the normalization
2. **when the outer edge of the elliptical ring touches the square in the numerator integral:** This happens when the semi-major axis of the outer ellipse is equal to 1, i.e. when  $c_1$  (or  $c_2$ ) = 5. This corresponds to the edge of the bumps in Fig. 3. As  $c$  gets smaller, the ellipses get more elongated and the area enclosed in the elliptical ring grows. When  $c = 5$ , this is still the case, but at some point as the ellipses start to

exit the square, the rate at which the area grows becomes matched and eventually overtaken by the rate at which area exits the square boundary. This explains the bump behavior.

3. **when the inner edge of the elliptical ring touches the square in the numerator integral:** This happens when the semi-major axis of the inner ellipse is equal to 1, i.e. when  $c_1$  (or  $c_2$ ) = 2.5. As  $c$  gets smaller after this, the region of integration corresponds to two separate curved bands; as the ellipses get stretched out further and further, they asymptotically get closer to looking like two flat rectangles. At this point, the axion with this small value of  $c$  is almost “decoupled” and irrelevant to the anthropic measure (although not quite, since there is still some curvature to the band for a while). This explains the asymptotic behavior of the curves in Fig. 3 at small  $c_2$ , rather than the exactly flat behavior when  $c_2 > 100$ .

## 1.4 $n$ axions

### 1.4.1 Thresholds

Following the discussion in Section 1.3.1, we can understand the interesting threshold regimes of Eq. (5) for  $n$  axions. In  $n$ -dimensions, the elliptical ring inside the square from the 2-dimensional case becomes an hyperellipsoidal (?) shell within a hypercube. ...

Range of intermediate  $c$ 's that we don't understand

### 1.4.2 Probability for $n$ axions with equal $c$ 's

The easiest case to consider for  $n$  axions is when all of them have the same  $c$ . In this case, the integrals in Eq. (5) reduce to 1-dimensional integrals in hyperspherical coordinates, over the radial coordinate ( $r \equiv \sum_a \theta_a^2$ ):

$$P = \mathcal{N}^{-1} \int_0^1 \frac{r^{n-1} dr}{1 + cr^2} \Theta(cr^2 - 2.5) \Theta(5 - cr^2) \quad (9)$$

Fig. 6 shows the result of Eq. (9) for chosen values of  $n$ . The behavior is as expected: as the number of axions increases, the probability drops to zero more and more quickly. The two regimes to notice are firstly, when  $c < 5$ , the axions are all light enough that we can ignore them in the anthropic measure, and secondly, when  $c > 100$ , the probability reaches its  $c$ -independent value, as calculated in [2]. These two thresholds are valid for all values of  $n$  (the second threshold when  $c > 100$  is not so obvious for larger  $n$ , but I checked this numerically.)

More quantitatively, for the values  $5 < c \leq 100$ , Eq. (9) evaluates to the following:

$$P = \frac{B(-2/5; 1 - n/2, 0) - B(-1/5; 1 - n/2, 0)}{B(-2/5; 1 - n/2, 0) - B(-1/c; 1 - n/2, 0)} \quad (10)$$



where  $B(x; a, b)$  is the incomplete beta function:  $\int_0^x t^{a-1}(1-t)^{b-1}dt$ . Also thought about perturbing away from equal  $c$ 's to get slightly different  $c$ 's for each axions; finding probability for scenarios where one group of axions has 1 value of  $c$  and the remaining have another value.

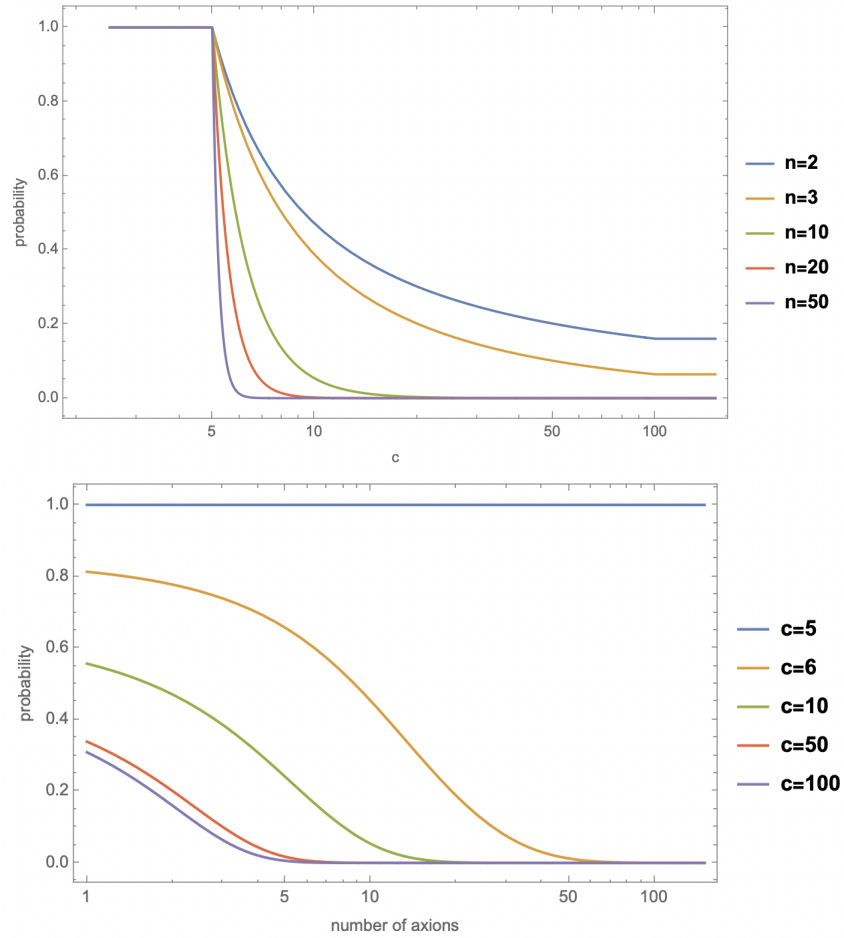


Figure 6: Top: Eq. (5) for different choices of  $n$  axions, where all axions have the same  $c$ . Bottom: Probability versus number of axions  $n$ , for chosen fixed values of  $c$ . For all values of  $c < 5$ , the probability curve lies on top of the blue curve, and for all values of  $c > 100$ , the curve lies on top of the purple curve.

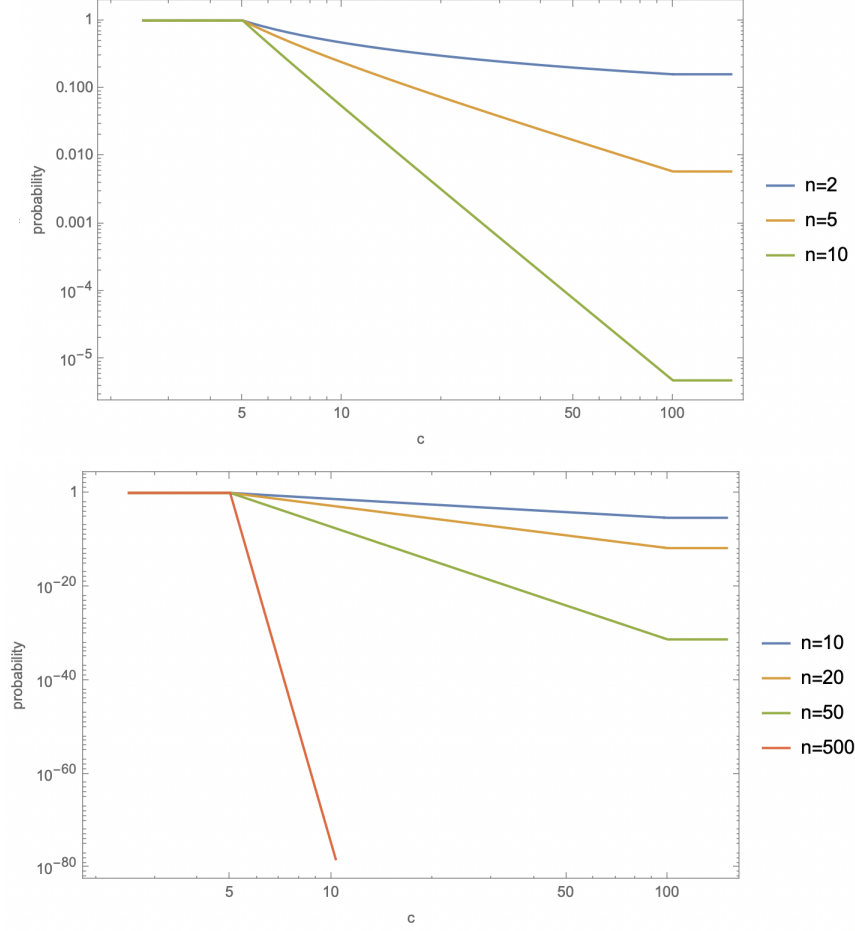


Figure 7: Same as Fig. 6 (probability vs. common  $c$ ) but on a log-log scale, and for larger values of  $n$ .

#### 1.4.3 Probability for $n$ axions in two $c$ regimes

Because the anthropic probability has these two regimes when  $c < 5$  and when  $c > 100$ , we can neglect the regime where  $5 < c < 100$  which we do not understand very well, and simplify the integrals in Eq. (5) as follows. If we are interested in  $n$  axions, and a fraction  $\mathcal{F}$  of them have  $c > 100$ , while a fraction  $1 - \mathcal{F}$  of them have  $c < 5$ , then we can separate the integration variables into two sets, such that the heavy ones can be written in spherical coordinates with  $r_1 \equiv \sum_{i=1}^{\mathcal{F}n} \theta_i^2$  and the light ones as  $r_2 \equiv \sum_{i=\mathcal{F}n+1}^n \theta_i^2$ . Then Eq. (5) can be written:

$$P = \mathcal{N}^{-1} \int_0^1 \int_0^1 \frac{r_1^{\mathcal{F}n-1} r_2^{(1-\mathcal{F})n-1} dr_1 dr_2}{1 + c_H r_1^2 + c_L r_2^2} \Theta(2.5 < 1 + c_H r_1^2 + c_L r_2^2 < 5) \quad (11)$$

where the normalization  $\mathcal{N}$  is the same integral but with the constraint  $2.5 < 1 + c_H r_1^2 + c_L r_2^2 < 100$ . This integral can be computed numerically and its result is shown in Fig. 8 below for  $n = 4$  and a few choices of  $\mathcal{F}$ .

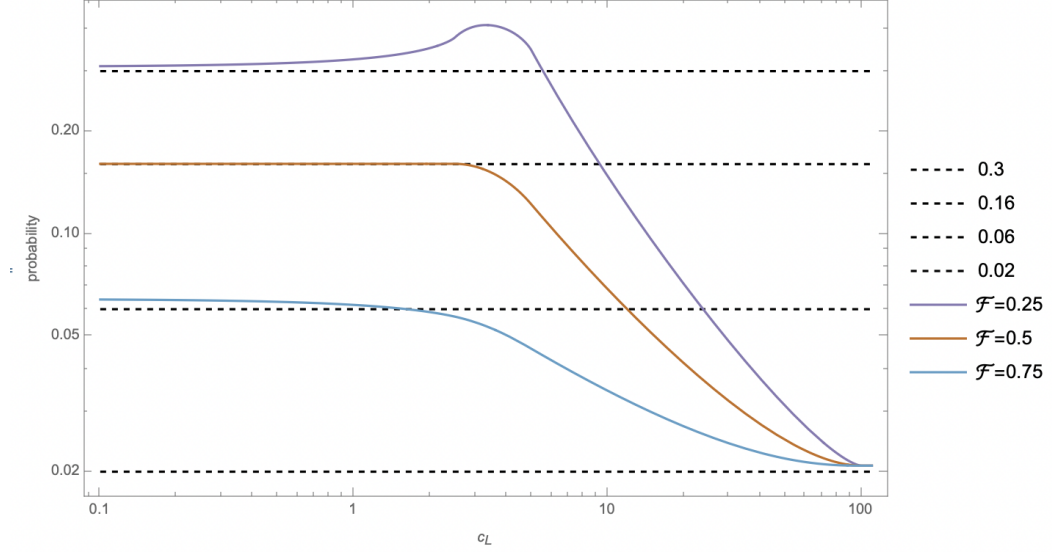


Figure 8: The result of Eq. (11) for  $n = 4$  and  $c_H = 100$ . The dashed lines show the probabilities for 1, 2, 3, and 4 axions contributing to the anthropic measure. The x-axis is  $c_L$  and the fraction of axions that have this value of  $c$  is given by  $1 - \mathcal{F}$ . If  $c_L > 100$ , we see the probability is equal to that of 4 axions for all choices of  $\mathcal{F}$ , while if  $c_L < 5$ , the probability approaches that for  $\mathcal{F}n$  axions for each chosen value of  $\mathcal{F}$  and  $n = 4$ .

We can therefore conclude that for all  $n$ , if an axion is light ( $c \lesssim 2.5 - 5$ ), it will not contribute to the anthropic measure, while if it is heavy ( $c > 100$ ), it will.

## 1.5 Allowed parts of parameter space

Eq. (8) tells us that certain choices of  $m, f$  and  $H_I$  will lead to an axion contributing to the anthropic probability. The plot below shows the part of parameter space that are allowed by anthropics for a single axion with mass  $m$  and decay constant  $f$ , for different fixed values of  $H_I$ . The part of parameter space that lies above the lines leads to values of  $c > 100$  and thus corresponds to parts of parameter space where the axion contributes to the anthropic measure.

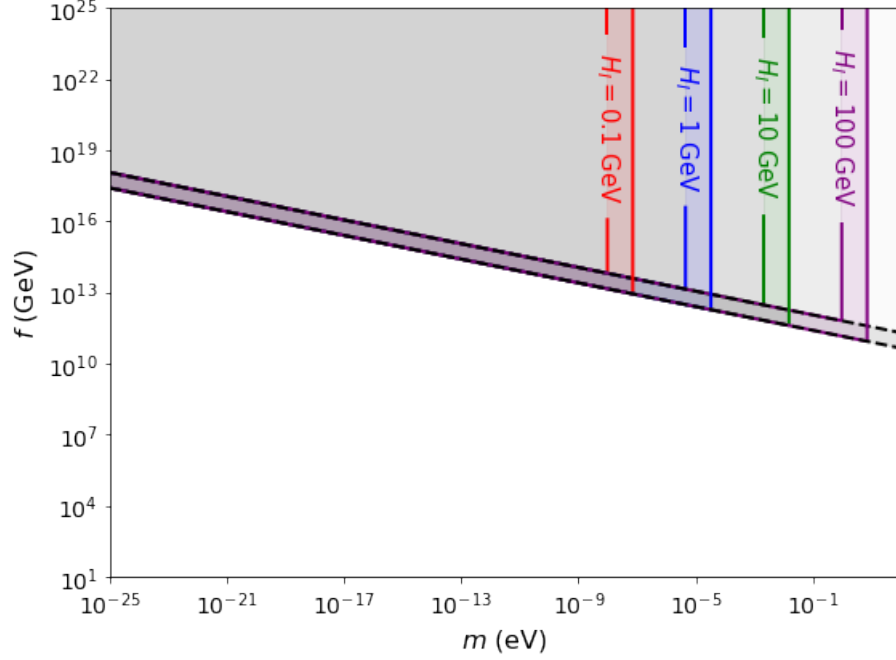


Figure 9: The grey shaded regions show the parts of parameter space that contribute to the anthropic probability, delimited by different colored lines corresponding to different choices of  $H_I$ . The white region corresponds to choices of axion parameters that do not contribute to the anthropic probability. The colorful bands correspond to the range  $5 < c < 100$  over which we do not really understand the contribution to the anthropic measure.

The black dashed line goes like  $m^{-1/4}$  and corresponds to Eq. (8) when  $\min \left\{ \pi^2, \frac{3H^4}{8\pi^2 m^2 f^2} \right\} = \pi^2$ , while the vertical lines correspond to the second case (which, notice in Eq. (8), leads to a value of  $c$  that does not depend on  $f$ ). The grey shaded region corresponds to the “anthropic region” for a given choice of  $H_I$ — the part of parameter space in which an axion would contribute to the anthropic measure. As the scale of inflation decreases, the anthropic region gets smaller since for low  $H_I$ , smaller misalignment angles are allowed, meaning that heavier axions can evade the requirement for contributing to the anthropic measure. The colorful shaded regions correspond to the intermediate range of  $c$ ’s for which we do not fully understand the probability distribution (i.e.  $5 < c < 100$ ). The white region of the plot correspond to choices of  $(m, f)$  which do not contribute to the anthropic measure.

### Things to do:

1. could include correction to the energy density from cosine potential in the probability calc
2. ~~what happens below  $c = \zeta_{\text{upper}}$ ?~~
3. ~~and related to the previous point, what is the bump? what does it look like with more axions?~~
4. ~~visualize/better understand the parts of parameter space that are viable via anthropics using Eq. (8)~~
5. keep in mind dependence of results on choice of measure (causal diamond vs others?)
6. how does Eq. (8) depend on number of axions?
7. fig 3 but same quantities plotted as fig 2 for easier comparison

## 2 Energy densities of 2 axions

David's simulations suggest that when there are couplings between many axions, the relic abundance in each axion no longer follow the expected  $m^{1/2}$  scaling that we expect from misalignment (see. Fig. 10 vs. Fig. 11).

Our goal is to determine if there really is energy redistribution among interacting axions and if so, what this process physically corresponds to. To do this, we'll start with two axions.

### 2.1 Gram-Schmidtification procedure

Consider a theory of two interacting axions  $\varphi_1/f_1 \equiv \theta_1$  and  $\varphi_2/f_2 \equiv \theta_2$  with a Lagrangian of the following form:

$$\mathcal{L} = \frac{1}{2}\partial_\mu\theta_1\partial^\mu\theta_1 + \frac{1}{2}\partial_\mu\theta_2\partial^\mu\theta_2 + \Lambda_b \cos(a\theta_1 + b\theta_2) + \Lambda_s \cos(c\theta_1 + d\theta_2) \quad (12)$$

where we can assume  $\Lambda_b > \Lambda_s$  and have set  $f_1 = f_2 = 1$  for now. The mixing matrix between the two fields can be written as follows:

$$A \equiv \begin{pmatrix} a & b \\ c & d \end{pmatrix} \quad (13)$$

Following the Gram-Schmidtification (GS) procedure, we want to perform a change of basis in order to rewrite this matrix as a lower triangular one, call it  $T$ . In other words, we are looking to redefine the fields in the above Lagrangian, so that the first cosine term contains only one redefined field, say  $\phi_1$ , while the second contains a linear combination of  $\phi_1$  and the second redefined field,  $\phi_2$ :

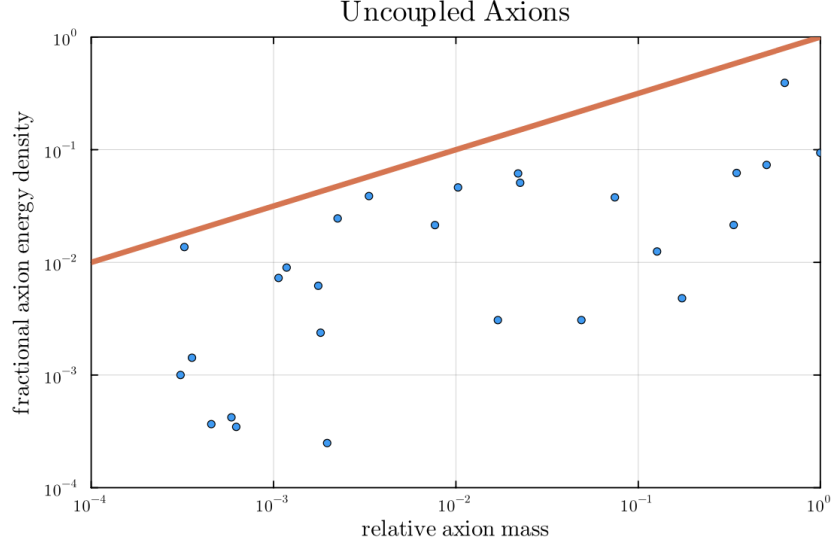


Figure 10: Energy density of 30 uncoupled axions. Each point corresponds to an axion of mass given by the x-axis (normalized to the heaviest axion) and energy density given by the y-axis (normalized by the total energy density).

$$\begin{cases} a\theta_1 + b\theta_2 = t_{11}\phi_1 \\ c\theta_1 + d\theta_2 = t_{21}\phi_1 + t_{22}\phi_2 \end{cases} \Leftrightarrow A \begin{pmatrix} \theta_1 \\ \theta_2 \end{pmatrix} = \begin{pmatrix} t_{11} & 0 \\ t_{21} & t_{22} \end{pmatrix} \begin{pmatrix} \phi_1 \\ \phi_2 \end{pmatrix} \quad (14)$$

We want to choose the  $d_{ij}$  so that the kinetic terms remain in canonical form after redefinition, so we will impose  $\frac{1}{2}\partial_\mu\theta_i\partial^\mu\theta_i = \frac{1}{2}\partial_\mu\phi_i\partial^\mu\phi_i$  and no cross terms. Dropping factors of 1/2 and derivatives for less cumbersome computation, we impose  $\theta_i^2 = \phi_i^2$ . Using Eq. (14), we write  $\theta_1$  and  $\theta_2$  in terms of the redefined fields:

$$\begin{pmatrix} \theta_1 \\ \theta_2 \end{pmatrix} = A^{-1}T \begin{pmatrix} \phi_1 \\ \phi_2 \end{pmatrix} \quad (15)$$

Using the matrices  $A$  and  $T$  as defined above, and then perform an inner product of this vector with itself to find:

$$\begin{aligned} \theta_1^2 + \theta_2^2 = \frac{1}{(\det A)^2} [ & \phi_1^2 (t_{21}^2 (a^2 + b^2) - 2t_{11}t_{21}(ac + bd) + t_{11}^2 (c^2 + d^2)) \\ & + 2t_{22}\phi_2\phi_1 (t_{21} (a^2 + b^2) - t_{11}(ac + bd)) + t_{22}^2\phi_2^2 (a^2 + b^2) ] \end{aligned}$$

The condition from the canonical kinetic terms means that we must impose:

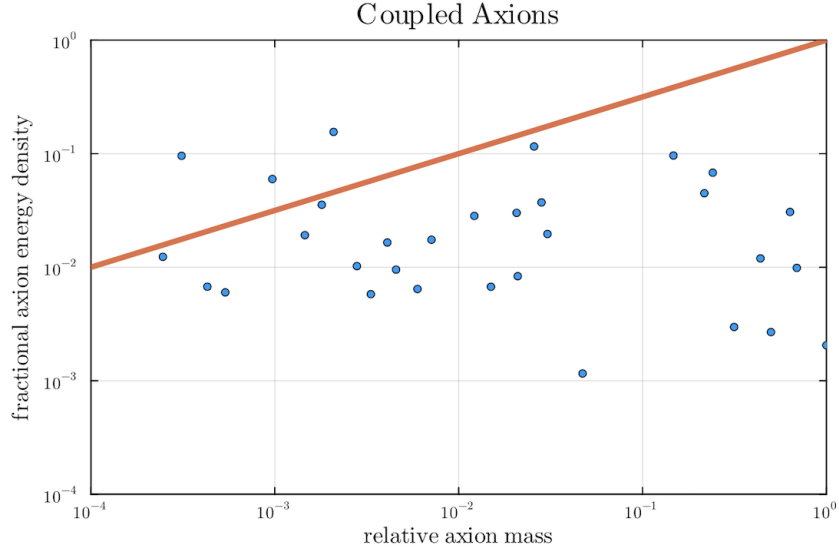


Figure 11: Energy density of 30 coupled axions. Same axes as above. It appears that the  $m^{1/2}$  scaling falls apart when interactions are present.

$$\begin{cases} \text{coefficient of } \phi_1^2 = (\det A)^{-2}((d - bx)^2 + (ax - c)^2) = 1 \\ \text{coefficient of } \phi_1\phi_2 = (\det A)^{-2}(2(d - bx)by - 2(ax - c)ay) = 0 \\ \text{coefficient of } \phi_2^2 = (\det A)^{-2}y^2(b^2 + a^2) = 1 \end{cases} \quad (16)$$

Solving for  $t_{ij}$ , we find:

$$\begin{cases} t_{11} = \sqrt{a^2 + b^2} \\ t_{21} = \frac{ca + db}{(\det A)^2} \\ t_{22} = \pm \frac{\det A}{\sqrt{a^2 + b^2}} \end{cases} \quad (17)$$

Thus, the Lagrangian is:

$$\begin{aligned} \mathcal{L} &= \frac{1}{2} \partial_\mu \phi_1 \partial^\mu \phi_1 + \frac{1}{2} \partial_\mu \phi_2 \partial^\mu \phi_2 + \Lambda_b \cos(\sqrt{a^2 + b^2} \phi_1) + \Lambda_s \cos\left(\frac{(ca + db)\phi_1 + \det A \phi_2}{\sqrt{a^2 + b^2}}\right) \\ &\sim \frac{1}{2} \partial_\mu \phi_1 \partial^\mu \phi_1 + \frac{1}{2} \partial_\mu \phi_2 \partial^\mu \phi_2 + \Lambda_b \cos(\sqrt{a^2 + b^2} \phi_1) + \Lambda_s \cos\left(\frac{\det A}{\sqrt{a^2 + b^2}} \phi_2\right) \end{aligned}$$

Because  $\Lambda_b > \Lambda_s$ ,  $\phi_1$  will receive the significant part of its dynamics from the first cosine term and so we can view this as the Lagrangian for two decoupled axions,  $\phi_1$  and  $\phi_2$ , each in their own cosine potential. The fields have a mass

hierarchy set by  $\Lambda_b > \Lambda_s$  and have decay constants rescaled from those of the original theory as follows:

$$\begin{cases} f_1 \rightarrow f_1/\sqrt{a^2 + b^2} \\ f_2 \rightarrow f_2(a^2 + b^2)/\det A \end{cases} \quad (18)$$

## 2.2 From interacting to “uncoupled” axions: relative energy densities

Now consider the slope,  $\gamma$ , in the  $\log(\rho_2/\rho_1)$  vs.  $\log(m_2/m_1)$  plane, where  $\rho_{1(2)} \sim m_{1(2)}^{1/2} (f_{1(2)} \theta_{i,1(2)})^2$  is the energy density in the decoupled fields  $\phi_{1(2)}$ , and  $m_{1(2)}$  is its mass. For uniformly distributed misalignment angles,  $\phi_{i,1(2)}$ , the expectation for this power law is given by:

$$\langle \gamma \rangle = \frac{\log(m_2^{1/2} f_2^2) - \log(m_1^{1/2} f_1^2)}{\log(m_2/m_1)} \quad (19)$$

After the GS procedure, we send the decay constants to their rescaled values as given in Eq. (18) and we find that we can write:

$$\langle \gamma \rangle = \frac{\log(F(m_2/m_1)^{1/2})}{\log(m_2/m_1)} \quad (20)$$

where  $F \equiv ((a^2 + b^2)/\det A)^2$  and we have set the decay constants  $f_1 = f_2 = 1$ . In our problem, the mixing coefficients  $\{a, b, c, d\}$  are each chosen from  $\{-1, 0, 1\}$  with equal probability. We would like to compute an average value of the power law, given that our potential is chosen at random in this manner. We find that there are only four possible values for  $F$ : 0, undefined, 1, 1/4. The cases where  $F = 0$  or  $F$  is undefined are not physically interesting as they correspond to cases where either the linear combinations in the cosine terms are linearly dependent, or where too many of these coefficients are zero, and so the fields may not appear at all in the potential, or may not be mixed. If these values of  $F$  are drawn, then we redraw mixing coefficients (if the potential had more cosine terms, this would be equivalent to moving to the cosine with the next largest  $\Lambda$ ). We can do this as many times as it takes to get  $F = 1$  or  $F = 1/4$ , which corresponds to a Markov chain process, and we can calculate the probability of ending up in these configurations by constructing a transition matrix, where the rows correspond to the incoming state, and the columns correspond to the outgoing state. As an example, I will work out the problem for the configuration/potential-choosing method outlined above.

There are 81 possible choices for the pairs  $(a, b)$  and  $(c, d)$ . Out of those 81, 24 correspond to cases where  $F = 0$ , 9 to  $F = \text{undefined}$ , 32 to  $F = 1$  and 16 to  $F = 1/4$ . The transition probability matrix is given by:



$$\mathbb{P} = \begin{pmatrix} 24/81 & 9/81 & 32/81 & 18/81 \\ 24/81 & 9/81 & 32/81 & 18/81 \\ 0 & 0 & 1 & 0 \\ 0 & 0 & 0 & 1 \end{pmatrix} \quad (21)$$

. Here, the choice of basis is such that the probabilities in a row or column correspond to the following order:  $(F = 0, F = \text{undefined}, F = 1, F = 1/4)$ . Notice that the rows add to 1 to conserve probability. The last two rows correspond to the fact that if we chose  $a, b, c$ , and  $d$  such that  $F = 1$  or  $1/4$ , then we do not re-draw. Probability theory tells us that:

$$P(X_t = j | X_0 = i) = (\mathbb{P}^t)_{ij} \quad (22)$$

and so we can calculate the probability of starting with either  $F = 0$  or undefined, and ending in either  $F = 1$  or  $1/4$  by looking at the appropriate entries of some high power of  $\mathbb{P}$ , which will end up converging to something close to:

$$\begin{pmatrix} 0 & 0 & 2/3 & 1/3 \\ 0 & 0 & 2/3 & 1/3 \\ 0 & 0 & 1 & 0 \\ 0 & 0 & 0 & 1 \end{pmatrix} \quad (23)$$

Therefore the overall probability of having either  $F = 1$  or  $F = 1/4$  is (this is bad notation, inconsistent with notation in Eq. (22) but anyway)

$$P(F = 1) = \frac{32}{81} + \frac{2}{3} \frac{24 + 9}{81} = \frac{54}{81} \quad (24)$$

$$P(F = \frac{1}{4}) = \frac{16}{81} + \frac{1}{3} \frac{24 + 9}{81} = \frac{27}{81} \quad (25)$$

where the second terms in the intermediate step of each line correspond to the contribution from choices of  $F = 0$  or undefined. We can therefore determine the weighted average of  $\langle \gamma \rangle$  using Eq. (20) as:

$$\begin{aligned} \langle \gamma \rangle_{GS} &= \frac{54}{81} \frac{1}{2} + \frac{27}{81} \frac{\log[(1/4)(m_2/m_1)^{1/2}]}{\log(m_2/m_1)} \\ &= \frac{1}{3} + \frac{27}{81} \left( \frac{-\log 4 + \frac{1}{2} \log(m_2/m_1)}{\log(m_2/m_1)} \right) \\ &\Rightarrow \langle \gamma \rangle_{GS} = \frac{1}{2} - \frac{1}{3} \frac{\log 4}{\log(m_2/m_1)} \end{aligned} \quad (26)$$

### 2.3 Comparing with simulation data

Consider again the most general potential for two interacting axions:

$$\mathcal{L} = \frac{1}{2} \partial_\mu \theta_i \partial^\mu \theta_i - [\Lambda_1^4 (1 - \cos(n_{11}\theta_1 + n_{12}\theta_2)) + \Lambda_2^4 (1 - \cos(n_{21}\theta_1 + n_{22}\theta_2))] \quad (27)$$

The below figure shows results from David's simulations: the y-axis shows the power law  $\gamma$  as defined in Eq. (19), for a given mass ratio  $1/\log(m_2/m_1)$ , given on the x-axis. Each point corresponds to a choice of potential, given in Eq. (27), where the  $n_{ij}$ 's are chosen at random from  $\{-1, 0, 1\}$  such that each field shows up at least once and each cosine is linearly independent. Each point (i.e. the outcome of a choice of potential) is averaged over 300 initial conditions for the misalignment angles.

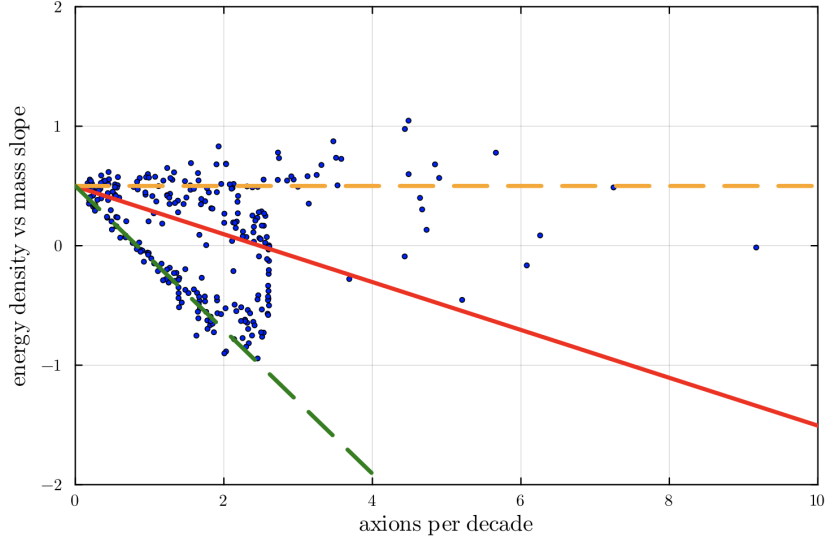


Figure 12: The vertical axis shows the power law  $\gamma = \log(\rho_2/\rho_1)/\log(m_2/m_1)$ , and the horizontal axis shows axions per decade of mass, or  $1/\log(m_2/m_1)$ . The red line is the line of best fit, which overlaps with the expression in Eq. (26). The green and orange line correspond to the two cases for the rescaled decay constants discussed in Section 2.2.

In Fig. 12, the red line corresponds to the line of best fit for the data points with axions per decade  $< 2$ . It also overlaps with the analytically calculated average given in Eq. (26). The orange line corresponds to the case where  $F = 1$ , and then green line corresponds to the case where  $F = 1/4$ , as discussed in Section. 2.2. See below Eq. (20) for the definition of  $F$ .

## 2.4 GSification generalized to N axions

Start with a Lagrangian of the form  $\frac{1}{2} k_{ij} \dot{\theta}_i \dot{\theta}_j + \sum_i \Lambda_i^4 (1 - \cos(n_{ij}\theta_j))$ , where we can assume that the  $\Lambda_i$  are ordered from largest to smallest. We can generalize

the procedure for 2 axions detailed in Section 2.1 to  $N$  axions (see David's note for details). We start by redefining the heaviest axion as  $\Phi_0 = n_{0i}\theta_i + \delta_0$  and all other axions as  $\Phi_\alpha = \theta_\alpha - c_\alpha\Phi_0$  where Greek indices start at 1 and Roman start at 0 and the  $c_\alpha$  coefficients depend on  $n_{ij}$  and  $k_{ij}$ . Once the Lagrangian is rewritten in terms of these variables and we enforce that the kinetic cross-terms between the 0-th and  $\alpha$ -th axions vanish, we find that  $c_\alpha = -Q_{0\beta}[Q^{-1}]_{\alpha\beta}$  (with  $Q$  defined below) and that the 0-th axion is kinetically decoupled from the others with a decay constant:

$$\frac{1}{2}f_0^2 = Q_{00} - Q_{0\alpha}Q_{0\beta}[Q^{-1}]_{\alpha\beta} \quad (28)$$

where the matrix  $Q$  is a symmetric ( $N \times N$ ) matrix, given by:

$$Q_{ij} = \begin{pmatrix} \frac{k_{00}}{n_{00}^2} & \frac{n_{0\alpha}n_{00} - k_{00}n_{0\alpha}}{n_{00}^2} \\ \frac{k_{0\alpha}n_{00} - k_{00}n_{0\alpha}}{n_{00}^2} & k_{\alpha\beta} - \frac{k_{0\alpha}n_{0\beta}}{n_{00}} - \frac{n_{0\alpha}n_{0\beta}}{n_{00}} + \frac{k_{00}n_{0\alpha}n_{0\beta}}{n_{00}^2} \end{pmatrix} \quad (29)$$

The remaining  $\alpha$ -th axions now have kinetic mixing matrix given by  $\tilde{k} = Q_{\alpha\beta}$  and potential mixing matrix:

$$\tilde{n}_{\alpha 0} = \frac{n_{\alpha 0}}{n_{00}} + (n_{\alpha\beta} - \frac{n_{\alpha 0}n_{0\beta}}{n_{00}})c_\beta \quad (30)$$

$$\tilde{n}_{\alpha\beta} = n_{\alpha\beta} - \frac{n_{\alpha 0}n_{0\beta}}{n_{00}} \quad (31)$$

These results can be fully rewritten in terms of matrix operations. If we define the ( $N \times N$ ) dimensional matrix

$$S \equiv \begin{pmatrix} 1/n_{00} & -n_{0\alpha}/n_{00} \\ 0 & \mathbb{1} \end{pmatrix} \quad (32)$$

then  $Q = S^T k S$  and the above results in Eqs. (28), and (30) become:

$$\tilde{n} = [S^T n S]_{\alpha\beta} \quad (33)$$

$$\tilde{k} = [S^T k S]_{\alpha\beta} \quad (34)$$

$$\frac{1}{2}f^2 = \frac{1}{[Q^{-1}]_{00}} \quad (35)$$

This procedure is repeated  $N$  times until every axion is independent. At each step, after GS-ification of the heaviest remaining field, we set the remaining interaction term between this heaviest axion and all the remaining ones (i.e. the term with coefficient  $\tilde{n}_{\alpha 0}$ ) to zero, as the dynamics of the heaviest axion are primarily determined by its own potential. In this way, the mixing matrices  $n$  and  $k$  decrease in dimension by 1 at each step, and the decay constant of the  $i$ -th axion is given by  $\frac{1}{2}(f_{(i)})^2 = 1/[(Q_{(i)})^{-1}]_{00}$ , where the lower index denotes the  $i$ -th axion.

### 2.4.1 Understanding scaling of $f$ as a function of $N$

We can numerically evaluate the  $f_{(i)}$ 's for some random choice of a symmetric, positive definite  $k_{ij}$  matrix and integer  $n_{ij}$  matrix. The plot below in Fig. 13 shows the decay constant of the  $i$ -th axion on the vertical axis after each step of GS-ification, against  $i$  on the horizontal axis, which indexes the axions from heaviest to lightest. In this example, the initial  $k_{ij}$  matrix is generated by first generating a diagonal  $N \times N$  matrix with random entries between  $[0, 1]$  (to ensure the matrix is positive definite), and then transforming it by a random element of  $SO(N)$ . The initial  $n_{ij}$  matrix is generated by randomly assigning an integer between  $[-10, 10]$  to each entry.

The general behavior of the curve is in agreement with the 2-axion result, where the lighter axion had an enhanced decay constant after GS-ification, while the heavier axion had a suppressed decay constant.

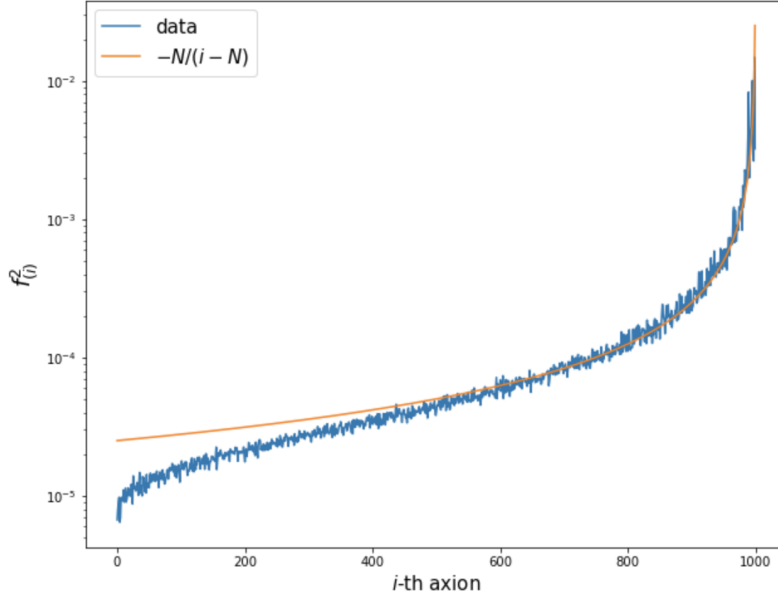


Figure 13: The blue curve shows the new decay constant of the  $i$ -th axion after the  $i$ -th iteration of the GS-ification procedure, plotted against  $i$ , which indexes the axions from heaviest to lightest. For the orange line, see Eq. (38) and the text around it.

To understand the general shape of the above curve, let's focus on the denominator of the expression for  $f_{(i)}^2$  given in Eq. (35). It can be shown that  $[Q^{-1}]_{00} \equiv [(S^T k S)^{-1}]_{00} = \vec{n}^T k^{-1} \vec{n}$  (see Ella's note), where  $\vec{n} \equiv n_{0i}$ . This can be rewritten in the following way:

$$\mathbb{E} [\vec{n}^T k^{-1} \vec{n}] = \text{tr} [k^{-1} \Sigma] + \vec{\mu}^T k^{-1} \vec{\mu} \quad (36)$$

where  $\Sigma = \vec{n} \cdot \vec{n}^T$  is the covariance matrix of  $\vec{n}$  and  $\vec{\mu}$  is the average value of  $\vec{n}$  (according to wikipedia, Quadratic form (Statistics)). Assuming that  $\vec{\mu} = 0$ , that  $\Sigma$  is roughly diagonal and does not change much between neighboring iterations, and that the primary difference between  $k$ 's of neighboring iterations (i.e.  $k_{(i+1)}$  and  $k_{(i)}$ ) is the difference in dimensionality (i.e. they are matrices of size  $(N-i) \times (N-i)$  and  $(N-i-1) \times (N-i-1)$  respectively), we can write the ratio of two successive decay constants post GS-ification as:

$$\frac{f_{(i+1)}^2}{f_{(i)}^2} \sim \frac{\text{tr} [(k_{(i)})^{-1} \Sigma]}{\text{tr} [(k_{(i+1)})^{-1} \Sigma]} \sim \frac{N-i}{N-i-1} \quad (37)$$

$$\Rightarrow f_{(i)}^2 \sim -\frac{N}{i-N} \quad (38)$$

The orange line shows this naive guess for the scaling of  $f_{(i)}^2$  with the  $i$ -th axion. It shows rather good agreement for a large number of axions  $N$ , but not at lower  $N$ . We're currently thinking about what could explain this part of the shape of the curve, and it doing so, we're thinking about what part of the assumptions outlined in the above paragraph are not quite true, starting with the last one. That is, we are thinking about how the  $k_{(i)}^{-1}$  matrix evolves over iterations and whether there is a large enough change in this evolution that would make the contribution from  $\text{tr} [(k_{(i)})^{-1}]$  more complicated than simply  $\sim N-i$

#### 2.4.2 An application of random matrix theory: understanding the evolution of the $k$ matrices over iterations

To actually understand what's going on, we need to understand how the distribution of the  $k$  matrix changes as we iterate through the GS-ification process.

The distribution of the  $k$  matrices seem to be following a two-sided exponential distribution (Laplace distribution), centered at zero:

$$f(x) = \frac{1}{2b} e^{-|x|/b} \quad (39)$$

#### Things to do:

1. understand where the triangle closes off, roughly at  $\text{ApD} \sim 2.5$
2. what happens for small mass separations where GS breaks down?
3. ~~generalize GS to N-axions~~ - need to understand results here
4. ~~generalize potentials (more general  $n_{ij}$  and allow for kinetic mixing)~~ - does the triangle fill in?

## A Introduction

Consider the general task of determining how the initial condition of a collection of scalar fields  $\boldsymbol{\theta}(0)$  maps onto the final partition of energy density among the various mass eigenstates, where the dynamics are controlled by the following Lagrangian:

$$\mathcal{L} = \frac{1}{2} \dot{\boldsymbol{\theta}}^T \mathbf{K} \dot{\boldsymbol{\theta}} - V(\boldsymbol{\theta}). \quad (40)$$

The kinetic term matrix  $\mathbf{K}$  may be diagonalized through the following field redefinition

$$\boldsymbol{\psi} \equiv \mathbf{F} \mathbf{R}^T \boldsymbol{\theta}, \quad \mathbf{F}^2 \equiv \mathbf{R}^T \mathbf{K} \mathbf{R}, \quad (41)$$

where  $\mathbf{R}^T \mathbf{R} = 1$ , and  $\mathbf{F}^2$  is the diagonal matrix of  $\mathbf{K}$  eigenvalues. In this basis, the Lagrangian becomes

$$\mathcal{L} = \frac{1}{2} \dot{\boldsymbol{\psi}}^T \dot{\boldsymbol{\psi}} - V(\mathbf{R} \mathbf{F}^{-1} \boldsymbol{\psi}). \quad (42)$$

Although one may as well have started with Equation (42), starting with Equation (40) is essential if the form of  $V$  is specified, since mixing induced by the off-diagonal kinetic terms will play an important role in the dynamics.

The potential  $V(\boldsymbol{\psi}) \equiv V(\mathbf{R} \mathbf{F}^{-1} \boldsymbol{\psi})$  is in general an arbitrarily complicated function of the fields, and it may have multiple, physically inequivalent minima, from which  $\boldsymbol{\psi}$  may be initialized arbitrarily far away. Therefore, at early times there is no sense in which one may define any particular linear combination of the fields to carry some definite fraction of the energy density of the system. Only at asymptotically late times is one guaranteed that the fields settle into a local minimum of the potential, though I emphasize that one does not know the location or curvature of this part of the potential *a priori*. Therefore, our algorithm to separate out the various late-time mass eigenstates of the fields must avoid making explicit reference to the shape of the potential about any particular point.

### A.1 Separable energy density

To simplify notation, we will use  $\mathbf{V}''$  and  $\mathbf{V}'$  to refer to the second and first derivatives  $\partial^2 V(\boldsymbol{\psi}) / \partial \psi \partial \psi$  and  $\partial V(\boldsymbol{\psi}) / \partial \psi$  respectively. The matrix  $\mathbf{V}''$  defines the square of the local mass eigenvalues, and so we must redefine the fields to work in the mass eigenstates:

$$\boldsymbol{\phi} \equiv \mathbf{S}^T \boldsymbol{\psi}, \quad \mathbf{M}^2 \equiv \mathbf{S}^T \mathbf{V}''(\boldsymbol{\psi}) \mathbf{S}, \quad (43)$$

where  $\mathbf{S}^T \mathbf{S} = 1$  and  $\mathbf{M}^2$  is the diagonal matrix of  $\mathbf{V}''(\boldsymbol{\psi})$  eigenvalues. The energy density contained in the field oscillations is then

$$\rho_{\text{tot}} \equiv \frac{1}{2} \dot{\boldsymbol{\phi}}^T \dot{\boldsymbol{\phi}} + \frac{1}{2} (\boldsymbol{\phi} - \boldsymbol{\phi}_0)^T \mathbf{M}^2 (\boldsymbol{\phi} - \boldsymbol{\phi}_0), \quad (44)$$

where  $\phi_0$  is the location of the minimum of the potential, which approximately satisfies

$$0 = \mathbf{V}''(\psi)(\psi - \psi_0) + \mathbf{V}'(\psi) = \mathbf{S}\mathbf{M}^2(\phi - \phi_0) + \mathbf{S}\mathbf{V}'(\phi) \quad (45)$$

Thus, the energy density is

$$\rho_{\text{tot}} \equiv \frac{1}{2}\dot{\phi}^T \dot{\phi} + \frac{1}{2}\mathbf{V}'(\phi)^T \mathbf{M}^{-2} \mathbf{V}'(\phi). \quad (46)$$

Labeling each of the mass eigenstates by their mass eigenvalue  $m$ , we may decompose the energy density:

$$\rho_m \equiv \frac{1}{2}\dot{\phi}_m^2 + \frac{1}{2}[\mathbf{M}^{-2}(\mathbf{V}'(\phi))^2]_m. \quad (47)$$

I assume a convention where the modes are sorted from lightest to heaviest, with  $m = m_0$  being the lightest eigenvalue and  $m_{-1}$  the heaviest.

## A.2 Pruning trivial modes

The procedure of Section A.1 is sufficient to determine the final partition of energy densities at asymptotically late times. In practice, integrating the equations of motion to very late times where one may assume that all states have settled to the bottom of some local minimum is impossible if the masses span more than a few orders of magnitude, since the number of time steps that must be taken is proportional to the ratio of the largest to smallest masses. On the other hand, heavy particles will settle to the minimum of their potential long before the lightest mass eigenstates have begun to oscillate, and so we may remove them from the integration by carefully checking that these modes are dynamically decoupled from all others.

To eliminate the heavy modes, it is enough to replace the damping term  $3H\dot{\phi}_{m_i}$  with the critically damped term  $2m_i\dot{\phi}_{m_i}$ . Note, though, that at every step, the heavy modes will still involve the heavy mass scale. Therefore, one should re-scale the heavy-mode EOM by the mass (squared) of the lightest mode that has been integrated out. This will keep the heavy modes dynamically forced to the bottom of their potentials, while removing any fast timescales.

## B Coupling to photons

In the interaction basis, there is a single mode that couples to photons, which we take to be  $\theta_1$  without loss of generality:

$$\mathcal{L}_{\text{int}} = \frac{\alpha_{\text{EM}}}{8\pi}\theta_1 \tilde{F}F = \frac{\alpha_{\text{EM}}}{8\pi}[\mathbf{R}\mathbf{F}^{-1}\mathbf{S}\phi]_1 \tilde{F}F. \quad (48)$$

For each mass eigenstate, the coupling to the photon is then given by the corresponding coefficient in the first row of this matrix.

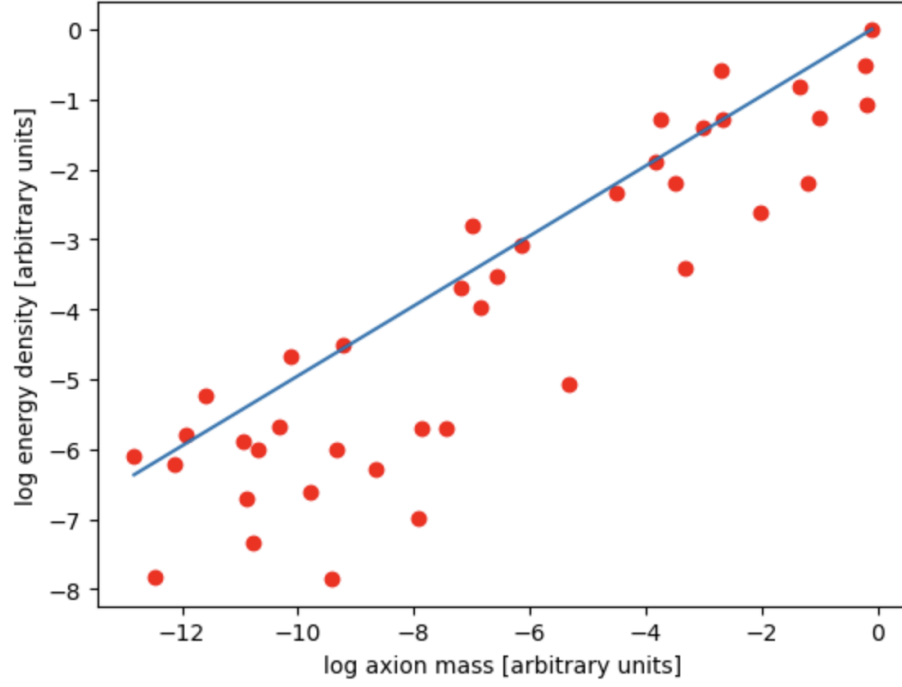


Figure 14: This is a simulation of the trivial case where each axion has its own instanton and the kinetic term is diagonal. The blue line represents the expectation that  $\rho \propto m^{1/2}$ . The horizontal axis is the log of the masses normalized against some arbitrary mass scale, while the vertical axis is the asymptotic relic abundance of each mass eigenstate normalized against some arbitrary energy density.



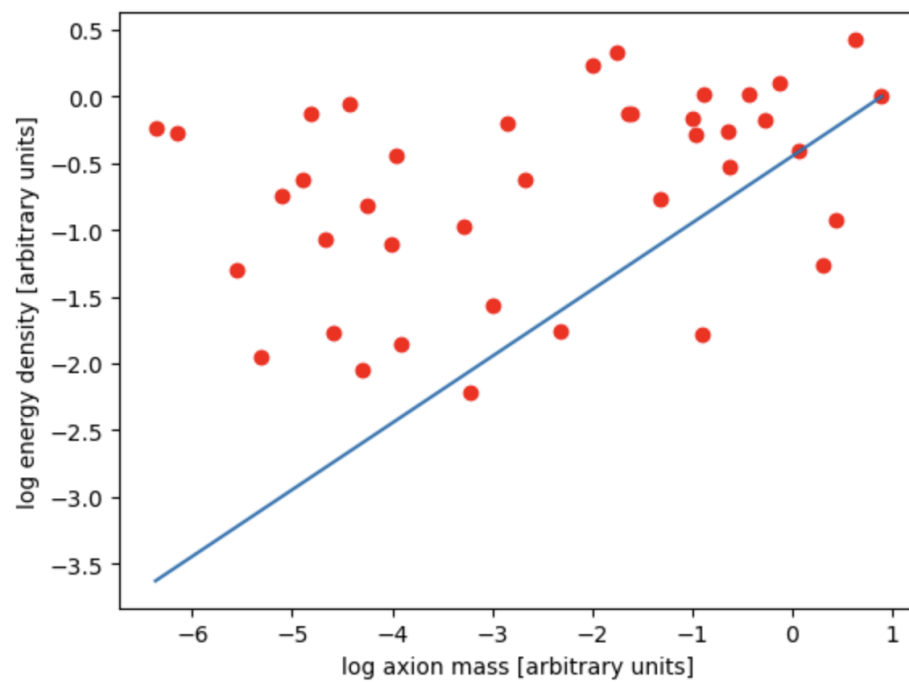


Figure 15: 40 axions!

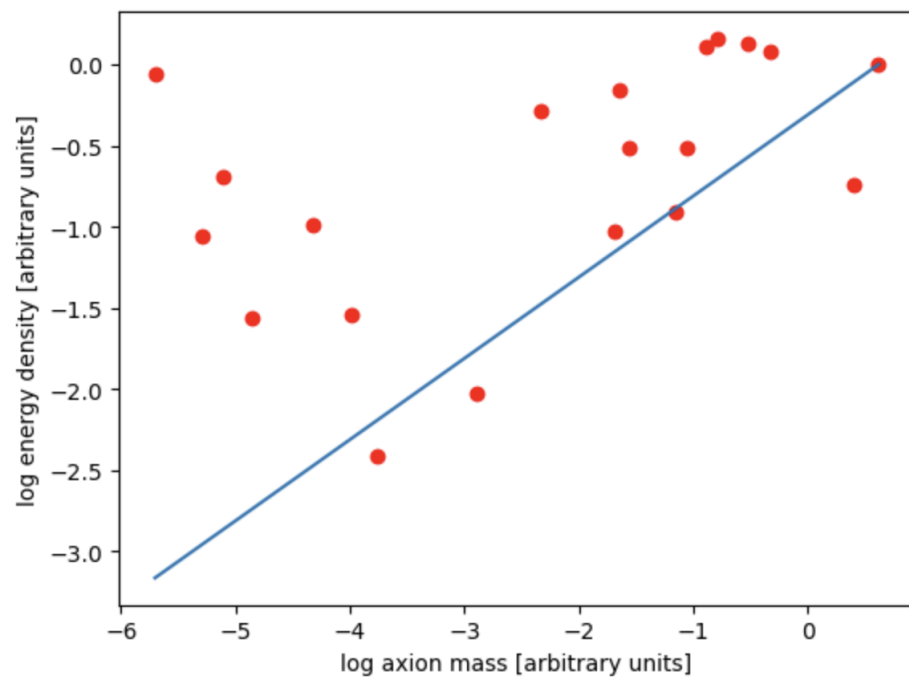


Figure 16: 20 axions!

## C Directions

1. Plot:  $g_{a\gamma\gamma}\sqrt{\rho/\rho_{\text{DM}}}$  vs mass (like what we have in the friendship paper) for all the axions.
2. Theoretical expectation for thermalization rate of nonlinearly coupled chain of oscillators – extend to time-varying parameters with adiabatic approximation
3. Theoretical expectations for the distribution of energy density among the mass eigenstates
4. Effect of QCD Axion?
5. Statistics of the CC (what is the distribution of vacuum energies?)

## D Being more clever

Let us consider the algorithm more carefully, and consider how it may be improved.

1. Heavy modes are still kept. Can we drop them entirely using an analytical method without introducing numerical error? Perhaps we simply don't include them in the rotation matrix?
2. Light modes are included in the rotation matrix even though they don't need to be included. Perhaps only including the oscillating modes in the rotation matrix would improve numerical stability.
3. In order to avoid using arbitrary precision during numerical integration, consider why arbitrary precision may be considered necessary at all. It is only the case that arbitrary precision would be necessary if terms with a huge dynamical range entered into the light field equations of motion in the first place. These terms necessarily cancel – how can we eliminate them without losing precision? IDEA: Suppose there are  $N$  dynamical degrees of freedom – using arbitrary precision, precompute an  $N$  dimensional subvolume of the potential

## References

- [1] B. Freivogel, “Anthropic Explanation of the Dark Matter Abundance,” *JCAP*, vol. 03, p. 021, 2010.
- [2] A. Arvanitaki and S. Dubovsky, “Exploring the string axiverse with precision black hole physics,” *Phys. Rev. D*, vol. 83, p. 044026, Feb 2011.